Obtaining acoustic intensity from multisource statistically optimized near-field acoustical holography

Trevor A. Stout, Alan T. Wall, Kent L. Gee, and Tracianne B. Neilsen

---

Articles you may be interested in

On the general connection between wave impedance and complex sound intensity
Proceedings of Meetings on Acoustics **30**, 055013 (2017); 10.1121/2.0000797

Precision device for measuring the three dimensional spectra of complex intensity
Proceedings of Meetings on Acoustics **30**, 055014 (2017); 10.1121/2.0000798

Gliding rippled spectrum discrimination: Ripple density and gliding velocity limits
Proceedings of Meetings on Acoustics **33**, 050001 (2018); 10.1121/2.0000801

Rating the perception of jet noise crackle
Proceedings of Meetings on Acoustics **33**, 040001 (2018); 10.1121/2.0000821

Properties of the ambient noise field at the 150-m isobath during the Canada Basin Acoustic Propagation Experiment
Proceedings of Meetings on Acoustics **33**, 070001 (2018); 10.1121/2.0000839

Robust real-time implementation of adaptive feedback cancellation using noise injection algorithm on smartphone
Proceedings of Meetings on Acoustics **33**, 055003 (2018); 10.1121/2.0000836

175th Meeting of the Acoustical Society of America

Minneapolis, Minnesota

7-11 May 2018

Signal Processing in Acoustics: Paper 1aSP3

Obtaining acoustic intensity from multisource statistically optimized near-field acoustical holography

Trevor A. Stout
Graduate Program in Acoustics, Pennsylvania State University. University Park, PA, 16802; stout.trevor.a@gmail.com

Alan T. Wall
Battlespace Acoust. Branch, Air Force Research Lab., Wright-Patterson AFB, OH; alan.wall.4@us.af.mil

Kent L. Gee and Tracianne B. Neilsen
Physics and Astronomy, Brigham Young University, Provo, UT; kentgee@byu.edu, tbnbyu@gmail.com

Multisource statistically optimized near-field acoustical holography (M-SONAH) improves the field reconstruction process by directly incorporating into the pressure propagator types of wavefunctions that correspond most closely to the source geometries of interest. The M-SONAH method has previously been used to localize acoustic sources in a full-scale jet engine plume above a rigid reflecting plane by adding a second set of cylindrical wavefunctions corresponding to the image source. Here, M-SONAH theory is extended to obtain the vector particle velocity and, by extension, the acoustic intensity. Discussed are two examples that relate to the full-scale jet noise-with-image-plane reconstruction problem: (1) a Gaussian line source with image and (2) a jet-like wavepacket and image, with hologram geometry identical to that of the full-scale experiment. The results from both examples reveal intensity errors less than 3 dB and 10 degrees within the top 20 dB of the reconstruction region. The results also suggest that intensity reconstruction magnitudes less than those obtained at the measurement aperture edges should be discarded.

1. INTRODUCTION

Some military personnel are exposed to high levels of jet noise from the current generation of fighter aircraft.[1] The effort towards jet noise reduction requires an understanding of the jet engine exhaust noise source, which is dominated by turbulent mixing noise.[2,3] The jet noise research community has applied inverse methods to characterize subsonic and supersonic jets. Microphones can be placed at multiple points outside of the jet plume and inverse methods are then used to infer source characteristics.[4,5] For example, one method called statistically-optimized near-field acoustical holography (SONAH)[6-8] allows for three-dimensional reconstruction of radiated acoustic fields. The SONAH technique was extended to account for multiple concurrent source geometries, with the modification termed multisource SONAH (M-SONAH).[9] This technique was then applied to image the near pressure field of a full-scale jet under static engine firing conditions in the presence of a rigid ground reflecting surface.[10] This paper describes further development of M-SONAH to allow for vector acoustic intensity field reconstructions in cylindrical geometries, describing both the magnitude and direction of sound energy flow. The method is tailored towards application to the same full-scale jet measurements and is here tested against two analytical test cases. The vectors obtained via holography compare favorably with the analytical results.

2. THE M-SONAH ALGORITHM

A. BACKGROUND

Near-field acoustical holography (NAH) techniques can produce reconstructions along a jet shear layer, elucidating the near-field behavior and directivity. Traditional NAH does so through the computation of spatial discrete Fourier transforms of the measurement hologram.[11] SONAH avoids some of the windowing effects of Fourier transforms[8] by instead calculating a spatial transfer function matrix between the hologram (measurement) locations and the reconstruction locations. To construct the transfer matrix (propagator), the measurement hologram and reconstruction locations are represented by a linear combination of spatial basis functions with coefficients determined via matrix inversion, such that a weighted summation of the functions matches the measured sound field in a least-norm sense. The field is reconstructed at a new location by summing the weighted wavefunction values there.

The SONAH algorithm is versatile, allowing for application to many different source and measurement geometries. Lee and Bolton used SONAH with a cylindrical hologram surrounding a subsonic jet, representing the sound field using cylindrical basis functions.[12] Their experiment was housed in an anechoic chamber, but SONAH may be adapted for measurements in non-free-field conditions, such as in the presence of reflective surfaces or two or more sources. For example, Hald included multiple sets of wavefunctions in the SONAH transfer function matrix through a straightforward concatenation scheme to account for both incoming and outgoing waves at a rigid boundary.[13] With two sets of cylindrical basis functions to represent a direct and reflected source, M-SONAH was previously applied to jet noise from a high-performance aircraft tethered to a concrete runway to produce pressure field reconstructions. Incorporation of two sets of cylindrical wavefunctions was shown to reconstruct ground reflection effects as expected in the full-scale measurement[9] and produces more accurate reconstructions than models which involve planar NAH[14].

The SONAH propagator for pressure can be modified to reconstruct the acoustic particle velocity field from complex pressure measurements. The pressure and particle velocity data can be combined to obtain the acoustic vector intensity field, providing additional information.[6-8,13,15] Hald's formulation of planar SONAH applies Euler's equation to calculate particle velocity in one direction from the reconstructed pressures[6,16]. Planar SONAH has also been used to reconstruct both pressure and particle velocity fields using measured particle velocities obtained with velocity probes, as shown by Jacobsen and Jaud[17]. If the pressures and particle velocities are measured concurrently, reconstructions can be obtained without the need for reference sensors according to the Broadband Acoustical Holography from Intensity Measurements (BAHIM) method.[18] A natural extension of the existing work is to modify a cylindrical M-SONAH algorithm to reconstruct particle velocity and acoustic intensity. This section describes the

development of such an algorithm, which is applied to measurements of a high-performance aircraft to reconstruct the intensity field near the aircraft in Section IV. For completeness, a summary of the derivation of M-SONAH is given based on the work of Wall[9], following which the modifications necessary for intensity reconstruction with multiple cylindrical basis functions are described.

B. FORMULATION

For a single frequency, the complex pressures at the hologram locations and at the reconstruction locations are expressed as a linear combination of complex pressure wavefunctions. The wavefunctions, $\psi_n, n = 1, 2, \ldots, N$, are chosen to correspond well to source geometries or to describe known properties of the field, which reduces the need for regularization (described below) and improves reconstruction accuracy compared to wavefunction sets that do not reflect the source geometry (see Refs. 7 and 16). To accomplish this, two matrices are formed, $\mathbf{A}(\mathbf{r}_h)$ and $\boldsymbol{\alpha}(\mathbf{r}_r)$, using the N wavefunctions evaluated at the measurement or hologram points, $\mathbf{r}_h$, and reconstruction locations, $\mathbf{r}_r$, respectively. That is,

$$\mathbf{A} = \begin{bmatrix} \psi_1(\mathbf{r}_{h,1}) & \psi_1(\mathbf{r}_{h,2}) & \cdots & \psi_1(\mathbf{r}_{h,M}) \\ \psi_2(\mathbf{r}_{h,1}) & \psi_2(\mathbf{r}_{h,2}) & & \psi_2(\mathbf{r}_{h,M}) \\ \vdots & & \ddots & \vdots \\ \psi_N(\mathbf{r}_{h,1}) & \psi_N(\mathbf{r}_{h,2}) & \cdots & \psi_N(\mathbf{r}_{h,M}) \end{bmatrix}, \boldsymbol{\alpha} = \begin{bmatrix} \psi_1(\mathbf{r}_{r,1}) & \psi_1(\mathbf{r}_{r,2}) & \cdots & \psi_1(\mathbf{r}_{r,L}) \\ \psi_2(\mathbf{r}_{r,1}) & \psi_2(\mathbf{r}_{r,2}) & & \psi_2(\mathbf{r}_{r,L}) \\ \vdots & & \ddots & \vdots \\ \psi_N(\mathbf{r}_{r,1}) & \psi_N(\mathbf{r}_{r,2}) & \cdots & \psi_N(\mathbf{r}_{r,L}) \end{bmatrix}, \quad (1)$$

where there are M hologram measurement points and L reconstruction points.

If two distinct sets of wavefunctions are used instead (e.g. to describe the effect of ground reflection), the matrices are formed by vertical concatenation. That is,

$$\mathbf{A} = \begin{bmatrix} \psi_1(\mathbf{r}_{h,1}) & \psi_1(\mathbf{r}_{h,2}) & \cdots & \psi_1(\mathbf{r}_{h,M}) \\ \psi_2(\mathbf{r}_{h,1}) & \psi_2(\mathbf{r}_{h,2}) & & \psi_2(\mathbf{r}_{h,M}) \\ \vdots & & \ddots & \vdots \\ \psi_N(\mathbf{r}_{h,1}) & \psi_N(\mathbf{r}_{h,2}) & \cdots & \psi_N(\mathbf{r}_{h,M}) \\ \psi'_1(\mathbf{r}_{h,1}) & \psi'_1(\mathbf{r}_{h,2}) & \cdots & \psi'_1(\mathbf{r}_{h,M}) \\ \vdots & & \ddots & \vdots \\ \psi'_N(\mathbf{r}_{h,1}) & \psi'_N(\mathbf{r}_{h,2}) & \cdots & \psi'_N(\mathbf{r}_{h,M}) \end{bmatrix}, \boldsymbol{\alpha} = \begin{bmatrix} \psi_1(\mathbf{r}_{r,1}) & \psi_1(\mathbf{r}_{r,2}) & \cdots & \psi_1(\mathbf{r}_{r,L}) \\ \psi_2(\mathbf{r}_{r,1}) & \psi_2(\mathbf{r}_{r,2}) & & \psi_2(\mathbf{r}_{r,L}) \\ \vdots & & \ddots & \vdots \\ \psi_N(\mathbf{r}_{r,1}) & \psi_N(\mathbf{r}_{r,2}) & \cdots & \psi_N(\mathbf{r}_{r,L}) \\ \psi'_1(\mathbf{r}_{r,1}) & \psi'_1(\mathbf{r}_{r,2}) & \cdots & \psi'_1(\mathbf{r}_{r,L}) \\ \vdots & & \ddots & \vdots \\ \psi'_N(\mathbf{r}_{r,1}) & \psi'_N(\mathbf{r}_{r,2}) & \cdots & \psi'_N(\mathbf{r}_{r,L}) \end{bmatrix}, \quad (2)$$

where ψ' denotes a member of the second set of wavefunctions. Any number of distinct wavenumber sets may be concatenated in this manner, representing any number of sources. The alternative definition of $\mathbf{A}$ and $\boldsymbol{\alpha}$ in Eq. (2) is central to the M-SONAH formulation.

The hologram and reconstruction pressures are formulated here as column vectors,

$$\mathbf{p}(\mathbf{r}_h) = \begin{bmatrix} p(\mathbf{r}_{h,1}) \\ p(\mathbf{r}_{h,2}) \\ \vdots \\ p(\mathbf{r}_{h,M}) \end{bmatrix}, \mathbf{p}(\mathbf{r}_r) = \begin{bmatrix} p(\mathbf{r}_{r,1}) \\ p(\mathbf{r}_{r,2}) \\ \vdots \\ p(\mathbf{r}_{r,L}) \end{bmatrix}, \quad (3)$$

and the wavefunctions must accurately represent the measured pressures according to the expansion

$$\mathbf{p}(\mathbf{r}_h) = \mathbf{A}^{\mathrm{T}} \mathbf{c}, \quad (4)$$

where $\mathbf{c}$ is a column vector of complex coefficients. The least-norm solution for the coefficients vector is found to be

$$\mathbf{c}^{\mathrm{T}} = \mathbf{p}(\mathbf{r}_h)^{\mathrm{T}} (\mathbf{A}^{\mathrm{H}} \mathbf{A})^{-1} \mathbf{A}^{\mathrm{H}}. \quad (5)$$

The M-SONAH prediction at the reconstruction location results from application of the least-norm solution for the coefficients vector to $\boldsymbol{\alpha}$,

$$\mathbf{p}(\mathbf{r}_r) \approx \mathbf{c}^{\mathrm{T}} \boldsymbol{\alpha} = \mathbf{p}(\mathbf{r}_h)^{\mathrm{T}} (\mathbf{A}^{\mathrm{H}} \mathbf{A})^{-1} \mathbf{A}^{\mathrm{H}} \boldsymbol{\alpha}. \quad (6)$$

If only one set of wavefunctions is used to build $\mathbf{A}$ and $\boldsymbol{\alpha}$, this formulation is equivalent to the traditional SONAH algorithm.[6-8,19]

To illustrate how the processing in M-SONAH is performed in the spatial domain, the matrix **a** is defined as

$$\mathbf{a} = (\mathbf{A}^{\mathrm{H}}\mathbf{A})^{-1}\mathbf{A}^{\mathrm{H}}\boldsymbol{\alpha}, \tag{7}$$

such that Eq. (6) becomes

$$\mathbf{p}(\mathbf{r}_r) \approx \mathbf{p}(\mathbf{r}_h)^{\mathrm{T}}\mathbf{a} \tag{8}$$

Like **A** and **α**, **a** is dependent only on the choice of wavefunctions and the geometry of the problem, so that once it is defined it may be used with any set of measured data $\mathbf{p}(\mathbf{r}_h)$ to compute reconstructed pressures at any location. Thus, **a** may be described as a spatial transfer function matrix.

The vector intensity may be found after computation of the particle velocity using the time-harmonic Euler's equation,

$$j\omega\rho_0\mathbf{u}(\mathbf{r}_r) = -\nabla\mathbf{p}(\mathbf{r}_r), \tag{9}$$

where j is the unit imaginary number, ω is the angular frequency, ρ_0 is the ambient density, $\mathbf{u}(\mathbf{r}_r)$ is the complex vector particle velocity at the reconstruction location, and $\nabla\mathbf{p}(\mathbf{r}_r)$ is the pressure spatial gradient with respect to the reconstruction location. In applying Euler's equation to the M-SONAH prediction for $\mathbf{p}(\mathbf{r}_r)$ in Eq. (6), note that $\mathbf{c}^{\mathrm{T}}$ does not depend on the reconstruction location $\mathbf{r}_r$ so the spatial gradient need only be applied to the matrix **α**, i.e.,

$$\mathbf{u}(\mathbf{r}_r) = \frac{j}{\omega\rho_0}\nabla\mathbf{p}(\mathbf{r}_r) \approx \mathbf{c}^{\mathrm{T}}\left(\frac{j}{j\omega\rho_0}\nabla\boldsymbol{\alpha}\right). \tag{10}$$

We see that calculation of the reconstructed particle velocity only requires manipulation of the matrix **α**. The vector intensities at the reconstruction locations are found from appropriate multiplication of the reconstructed pressures and velocities,

$$\mathbf{I}(\mathbf{r}_r) = \frac{1}{2}\mathrm{Re}(\mathbf{p}(\mathbf{r}_r)\mathbf{u}(\mathbf{r}_r)^*) \approx -\frac{1}{2\omega\rho_0}\mathrm{Im}\big(\mathbf{c}^{\mathrm{T}}\boldsymbol{\alpha}\mathbf{c}^{\mathrm{H}}\nabla\boldsymbol{\alpha}^*\big), \tag{11}$$

where the operator Re denotes the real part, Im the imaginary part, and ∗ the complex conjugate. Thus, the three-dimensional intensity reconstruction can be calculated via Eq. (11) in one numerical step.

C. REGULARIZATION

To account for the amplification of high-order evanescent-like waves and other factors such as spatial noise in $\mathbf{p}(\mathbf{r}_h)^{\mathrm{T}}$ caused by variability in microphone placement, the inverse of $\mathbf{A}^{\mathrm{H}}\mathbf{A}$ is typically regularized in Eqs. (5) – (7). Williams[20] provides several regularization methods for NAH, including application of a modified Tikhonov filter to the matrix inversion. Cho et al.[7] and Wall et al.[9] further describe this technique applied to SONAH. After a singular value decomposition giving

$$\mathbf{A}^{\mathrm{H}}\mathbf{A} = \mathbf{V}\mathbf{G}\mathbf{V}^{\mathrm{H}}, \tag{12}$$

the modified Tikhonov filter, $\mathbf{F}_1^{\alpha}$, may be used to obtain the regularized inverse of $\mathbf{A}^{\mathrm{H}}\mathbf{A}$,

$$\mathbf{R}_{\mathbf{A}^{\mathrm{H}}\mathbf{A}} = \mathbf{V}\big(\alpha(\mathbf{F}_1^{\alpha}) + \mathbf{G}^{\mathrm{H}}\mathbf{G}\big)^{-1}\mathbf{G}^{\mathrm{H}}\mathbf{V}^{\mathrm{H}}, \tag{13}$$

where $\mathbf{F}_1^{\alpha}$ is given by

$$\mathbf{F}_1^{\alpha} = \mathrm{diag}\left[\ldots, \frac{\alpha}{\left[\alpha + |\lambda_i|^2\left(\frac{\alpha + |\lambda_i|^2}{\alpha}\right)^2\right]}, \ldots\right], \tag{14}$$

where α is a regularization parameter and λ_i is the ith singular value found along the diagonal of **G**. The regularization parameter α is found by minimizing the cost function,

$$J(\alpha) = \frac{\left\|\mathbf{F}_1^{\alpha}\mathbf{V}^{\mathrm{H}}\mathbf{p}(\mathbf{r}_h)\right\|^2}{[\mathrm{trace}(\mathbf{F}_1^{\alpha})]^2}. \tag{15}$$

This filters out noise in the higher-order terms of the field decomposition.

The complete SONAH algorithm, including the regularized inverse, computes the wavefunction coefficients vector and reconstructed intensity as

$$\mathbf{c}^{\mathrm{T}} = \mathbf{p}(\mathbf{r}_h)^{\mathrm{T}}\, \mathbf{R}_{\mathbf{A}^{\mathrm{H}}\mathbf{A}}\mathbf{A}^{\mathrm{H}}, \quad \mathbf{I}(\mathbf{r}_r) \approx -\frac{1}{2\omega\rho_0}\,\mathrm{Im}\big(\mathbf{c}^{\mathrm{T}}\boldsymbol{\alpha}\mathbf{c}^{\mathrm{H}}\nabla\boldsymbol{\alpha}^*\big). \tag{16}$$

The pressure and particle velocity have the same formulation as above, differing from Eqs. (6) and (10) only by this new definition of $\mathbf{c}^{\mathrm{T}}$.

D. CYLINDRICAL GEOMETRY

We now explicitly define the above formulation in Eqs. (2)-(16) with a cylindrical geometry, corresponding to our choice of two sets of cylindrical wavefunctions to describe the jet and its image source. The two sets have central axes corresponding to the physical jet axis and the image source axis of the jet, respectively, following the scheme of Wall, *et al.*[10] This section builds on their work, towards a particle velocity and intensity reconstruction of the same sound field. Elementary cylindrical pressure wavefunctions at location (r, φ, z) are given by

$$\psi_{k_z,n}(r,\varphi,z) = \frac{H_n^{(1)}(k_r r)}{H_n^{(1)}(k_r r_s)}e^{jn\varphi}e^{jk_z z}, r \geq r_0, \tag{17}$$

where $H_n^{(1)}$ is the nth-order Hankel function of the first kind, r_s is some small reference radius or assumed source radius. The radial wavenumber, k_r, is dependent on the axial wavenumber, k_z, and the wavenumber of interest, $k = \frac{\omega}{c}$, (where ω is the angular frequency and c is the ambient sound speed), by

$$k_r = \begin{cases} \sqrt{k^2 - k_z^2}, |k| \geq |k_z|, \\ \sqrt{k_z^2 - k^2}, |k| < |k_z|. \end{cases} \tag{18}$$

The two sets of these wavefunctions are evaluated at the hologram locations to form ψ_i and ψ'_i using Hankel functions of order $n = 0$ (assuming axisymmetric sources), then concatenated into $\mathbf{A}$. The wavefunction sets are similarly evaluated at the reconstruction locations to form $\boldsymbol{\alpha}$.

Each component of particle velocity may be calculated individually in the SONAH formulation. For convenience, we define a set of particle velocity cylindrical wavefunction matrices as

$$\boldsymbol{\alpha}_r = -\frac{1}{j\omega\rho_0}\nabla_r\boldsymbol{\alpha}, \qquad \boldsymbol{\alpha}_\varphi = -\frac{1}{j\omega\rho_0}\nabla_\varphi\boldsymbol{\alpha}, \qquad \boldsymbol{\alpha}_z = -\frac{1}{j\omega\rho_0}\nabla_z\boldsymbol{\alpha}, \tag{19}$$

where $\nabla_i\boldsymbol{\alpha}$ is defined as the component of the cylindrical gradient with respect to the reconstruction location acting on each entry of $\boldsymbol{\alpha}$, or

$$\nabla_i\boldsymbol{\alpha} = \begin{bmatrix} \nabla_i\psi_1(\mathbf{r}_{r,1}) & \nabla_i\psi_1(\mathbf{r}_{r,2}) & \cdots & \nabla_i\psi_1(\mathbf{r}_{r,L}) \\ \nabla_i\psi_2(\mathbf{r}_{r,1}) & \nabla_i\psi_2(\mathbf{r}_{r,2}) & & \nabla_i\psi_2(\mathbf{r}_{r,L}) \\ \vdots & & \ddots & \vdots \\ \nabla_i\psi_N(\mathbf{r}_{r,1}) & \nabla_i\psi_N(\mathbf{r}_{r,2}) & \cdots & \nabla_i\psi_N(\mathbf{r}_{r,L}) \\ \nabla_i\psi'_1(\mathbf{r}_{r,1}) & \nabla_i\psi'_1(\mathbf{r}_{r,2}) & \cdots & \nabla_i\psi'_1(\mathbf{r}_{r,L}) \\ \vdots & & \ddots & \vdots \\ \nabla_i\psi'_N(\mathbf{r}_{r,1}) & \nabla_i\psi'_N(\mathbf{r}_{r,2}) & \cdots & \nabla_i\psi'_N(\mathbf{r}_{r,L}) \end{bmatrix}. \tag{20}$$

With this definition, the three components of reconstructed particle velocity are found to be

$$\mathbf{u}_r \approx \mathbf{c}^{\mathrm{T}}\boldsymbol{\alpha}_r, \qquad \mathbf{u}_\varphi \approx \mathbf{c}^{\mathrm{T}}\boldsymbol{\alpha}_\varphi, \ \text{ and } \ \mathbf{u}_z \approx \mathbf{c}^{\mathrm{T}}\boldsymbol{\alpha}_z. \tag{21}$$

The components of the gradient of the wavefunctions are found to be[21]

$$\nabla_r\psi_{k_z,n}(r,\varphi,z) = \frac{k_r}{2}\frac{H_{n-1}^{(1)}(k_r r) - H_{n+1}^{(1)}(k_r r)}{H_n^{(1)}(k_r r_s)}e^{jn\varphi}e^{jk_z z}, \tag{22}$$

$$\nabla_\varphi\psi_{k_z,n}(r,\varphi,z) = \frac{jn}{r}\psi_{k_z,n}(r,\varphi,z), \tag{23}$$

$$\nabla_z\psi_{k_z,n}(r,\varphi,z) = jk_z\psi_{k_z,n}(r,\varphi,z), \tag{24}$$

where ρ_0 is the ambient density. Equations (22) through (24), together with the pressure wavefunctions in Eq. (17), give the complex values of the entries of $\boldsymbol{\alpha}_r$, $\boldsymbol{\alpha}_\varphi$, and $\boldsymbol{\alpha}_z$ in Eqs. (19) and (21).

For geometries with multiple origins or central axes, such as a direct jet source and image jet source, one complication arises from the vector nature of the particle velocity. While the pressure wavefunctions are scalar, the particle velocity wavefunctions are vector, and the r, φ, and z components depend on the choice of central axis. The components of the particle velocity and thus the intensity predicted by the M-SONAH algorithm are referenced to this same axis. Thus, if two sets of cylindrical wavefunctions are used, care must be taken to ensure that the individual components reference a common z-axis before they may be concatenated to form the matrices $\boldsymbol{\alpha}_r$, $\boldsymbol{\alpha}_\varphi$, and $\boldsymbol{\alpha}_z$. One way to achieve this with two sets of cylindrical wavefunctions is to calculate the sets with respect to two different z-axes as an intermediate step, (e.g. the direct source axis and an image source axis behind a planar reflecting surface), and then project the components of one of the sets into the coordinate system of the other set. For the case of a planar reflecting surface, the two z-axes will be parallel, so only the r and φ components need to be projected.
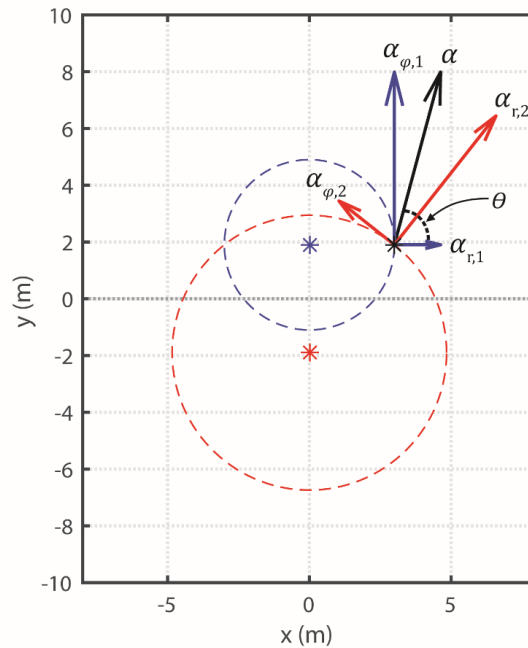

Figure 1. Wavefunction vector α located at $x = 3$ m, $y = 1.9$ m decomposed into r and φ components with respect to two cylindrical coordinate systems. The two z axes are parallel and out of the page, located at $y = 1.9$ and $y = -1.9$ m, and the dashed circles are centered around these axes. These systems correspond to a hypothetical direct source and image source, formed from a rigid planar surface at $y = 0$.

An example of a single particle velocity wavefunction vector with r and φ components $\alpha_{r,2}$ and $\alpha_{\varphi,2}$, being projected into the coordinate system of another wavefunction set is illustrated in Fig. 1. For convenience, though the wavefunction values are in general complex, only the real parts are depicted in the figure. The two wavefunction sets correspond to a hypothetical direct and image source, with z-axes at $y = 1.9$ m and $y = -1.9$ m respectively and at $x = 0$ m (shown by blue and red stars), where $y = 0$ describes a planar rigid surface. The dashed circles in Fig. 1 intersect at a reconstruction location at $x = 3$, source coordinate system, with components $\alpha_{r,2}$ and $\alpha_{\varphi,2}$ shown with red arrows. The angle θ is between α and the vector component $\alpha_{r,1}$ with respect to the direct source coordinate system. The components $\alpha_{r,1}$ and $\alpha_{\varphi,1}$, (shown in blue) may be calculated via the following steps for each of the real parts and imaginary parts: First, calculate the magnitude of the real part or imaginary part of the vector (i.e. the length of the black vector in Fig. 1) from the component values; second, find the angle θ using the dot product formula,

$$\theta = \cos^{-1}\left(\frac{\alpha \cdot \hat{r}_1}{|\alpha|}\right), \tag{25}$$

where $\hat{r}_1$ is the unit vector in the r direction with respect to the direct source (found using the reconstruction point coordinates); third, compute $\alpha_{r,1}$ and $\alpha_{\varphi,1}$ according to the formulae,

$$\alpha_{r,1} = |\alpha| \cos\theta, \tag{26}$$

$$\alpha_{\varphi,1} = |\alpha| \sin\theta. \tag{27}$$

Note that there are many different methods for finding $\alpha_{r,1}$ and $\alpha_{\varphi,1}$. Equations (25)-(27) must be applied to both the real and imaginary parts of the vectors, then the results are combined to find the complex values that are ultimately included in the matrices $\boldsymbol{\alpha}_r$ and $\boldsymbol{\alpha}_\varphi$ in Eq. (19) to reconstruct particle velocity via Eq. (21).

3. ANALYTICAL TEST CASES

The performance of the cylindrical geometry M-SONAH algorithm for intensity reconstruction is tested in this section in two different scenarios simulating acoustic measurement of dual line arrays of monopoles as a simple model of a jet source with an image source. The first scenario is a general case where the ability of M-SONAH to predict intensity both inwards and outwards is demonstrated. The second involves the specific measurement geometry used in the full-scale jet sound field referenced above.[10] In both cases, the simulated pressure measurements used as inputs to the M-SONAH algorithm are calculated using Green's functions to represent complex pressures radiated from the sources defined below. Random variations are added to represent noise measurements with a signal-to-noise ratio of 60 dB. Both the M-SONAH predicted intensity magnitudes and vector directions are compared to the analytical calculation. The only source information provided *a priori* to the algorithm is the location of the simulated line array axes; thus, the performance here gives an indication of the algorithm's real-world performance.

A. SIMPLE GEOMETRY

This scenario is designed to assess the ability of M-SONAH to reconstruct vector intensity at points closer to and farther away from the hologram location, with respect to the source location. The analytical source is made up of two coherent line arrays of monopoles in the z-y plane extending from $z = -5$ to 5 m, along $y = 5$ m and $y = -5$ m, respectively, at a frequency of 100 Hz. The magnitudes of the monopole complex source strengths, Q, follow a Gaussian distribution with distance, and the spacing between monopoles is small (about $1/15^{th}$ of a wavelength) so that the arrays resemble two line sources. The two line sources are equal in amplitude to simulate both a direct and image source with a perfectly rigid boundary and the sources are all perfectly in phase.

The pressure and vector particle velocity for a group of coherent monopoles are given by

$$p(\boldsymbol{r}) = \sum \frac{jQ\rho_0 ck}{4\pi R} e^{-jkR}, \tag{28}$$

$$\boldsymbol{u}(r) = \sum \frac{jQk}{4\pi R}\left(1 - \frac{j}{kR}\right)e^{-jkR}\hat{R}, \tag{29}$$

where R is the distance between the field point $\boldsymbol{r}$ and the source point, $\hat{R}$ is the unit vector pointing from source to field point, Q is the complex source strength, and the summation is taken over the individual monopoles. The sound speed is chosen to be $c = 343$ m/s and k is the acoustic wavenumber. Vector intensity is found from the appropriate multiplication (see the first equality in Eq. (11)) of the two complex quantities found in Eqs. (28) and (29).

The M-SONAH algorithm begins with the analytically-calculated complex pressures (with 60 dB SNR) at a plane at $x_h = 2$ m away from the source plane, and at 1-m spacing in y and z, with an aperture of 20 m by 20 m in the y-z plane. The algorithm then predicts the vector intensities at two planes, at $x = 0.1$ m and 5 m, using cylindrical wavefunctions with z axes corresponding to the locations of the line sources. Figure 2 shows the source geometry and the locations of the reconstruction planes. The intensity reconstructions are shown in Fig. 3 and errors in magnitude and vector angle are detailed in Figs. 4-5. For Figs. 3-5, only the reconstruction planes are shown, though in Fig. 3 the sound intensity level (L_I) values are shown relative to the maximum level on the measurement plane. For purposes of illustration in both scenarios, only a few intensity vectors are shown, although the grid spacing is much finer. In Fig. 3, the base of each arrow

indicates the intensity reconstruction locations, while the color map and arrow lengths indicate L_I. In Figs. 4 and 5, the color map indicates reconstruction error in level or angle with reference to the analytically calculated values.
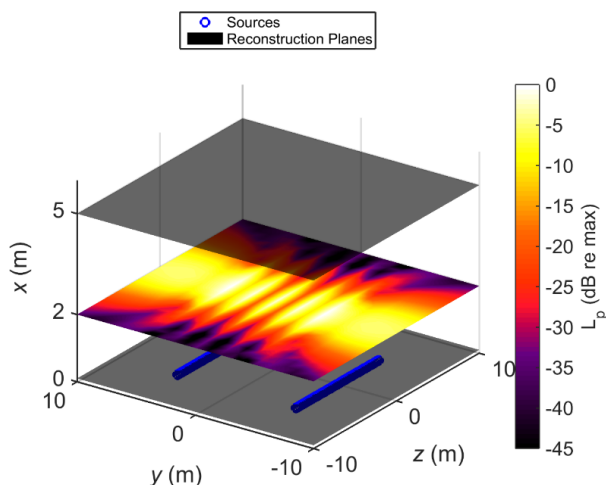

Figure 2. Geometry of numerical simulation and simulated measurement hologram. Transparent planes indicate where data are to be reconstructed. Source monopole locations are indicated by circles; their spacing is close enough that they resemble two line sources.
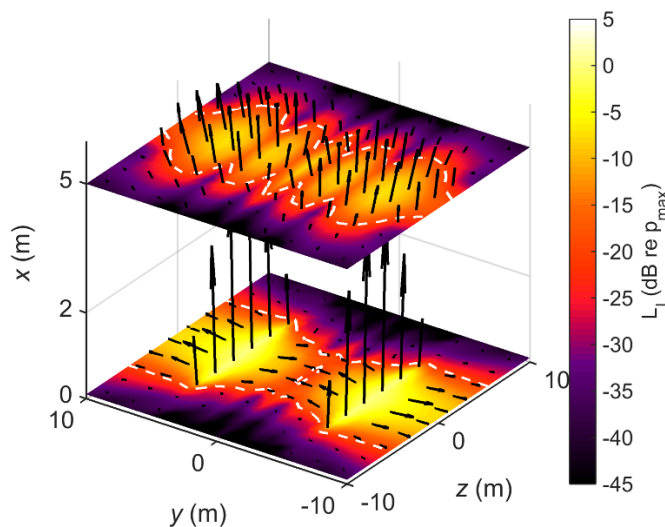

Figure 3. Sound intensity reconstructed at x = 0.1 m and x = 5 m from the source plane from the complex pressure hologram at x_h = 2 m (not shown). Inside the dashed contour lines L_I is within 20 dB of the maximum reconstructed level at each plane.

The intensity reconstruction in Fig. 3 illustrates constructive and destructive interference between the two line arrays. Along both reconstruction planes and most notably at $x = 5$ m, multiple intensity lobes are separated by clear spatial nulls, and the vector intensity y-component varies between the lobes. These nulls and vector directions are accurate with respect to the analytical calculations, as can be seen from the low magnitude error in Fig. 4 and low angle error in Fig. 5. For the top 20 dB with respect to the measurement plane, errors in magnitude are less than about 3 dB, and errors in vector angle are less than about ten degrees, both inward and outward from the hologram location (higher errors can be seen outside the dashed lines where the reconstructed intensity magnitudes are below 20 dB of the maximum, near $z = \pm 10$ m). Interference from ground reflections is inevitable in any measurement where the source and receiver are both off the ground; thus, this reconstruction shows the feasibility of applying M-SONAH to such

measurements. It is the application of two cylindrical sets of wavefunctions which allows M-SONAH to capture these important features.

In general, this simulation illustrates the accuracy of the M-SONAH algorithm in predicting the top 20 dB of vector intensity from line sources, given a sufficiently high signal to noise ratio and large aperture. The performance of M-SONAH when a more limited aperture is used in the measurement is described by the simulation in the second scenario, detailed in the next section.
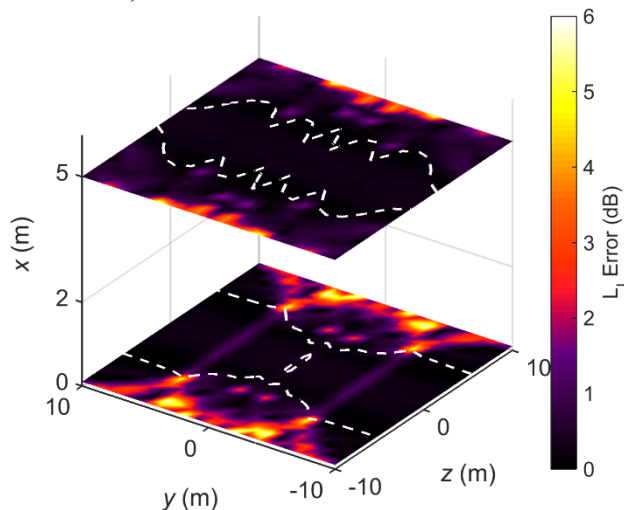
Figure 4.   Sound intensity level error between the reconstructed and simulated intensities. Note how the reconstruction has less than 3 dB error in L_I at nearly all points where the L_I is within 20 dB of the maximum on that plane (i.e., inside the dashed lines).
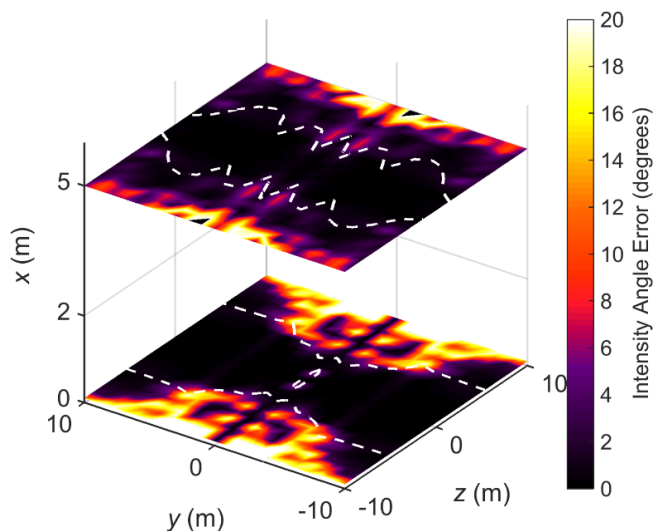

Figure 5. Angle error between the reconstructed and simulated intensities. The color axis is pinned to 20° maximum error for clarity. Note how the reconstruction has less than 10° error in the direction of the intensity at nearly all points where the L_I is within 20 dB of the maximum on that plane (i.e., inside the dashed lines).

B.   SIMULATION OF FULL-SCALE JET GEOMETRY

In the second scenario, two line sources are positioned along the jet axis and image jet axis corresponding to the actual full-scale jet measurements mentioned previously[10], again at 100 Hz. The complex amplitudes along the line sources are spatially shaped by a hyperbolic tangent function proposed by Papamoschou[22] based on a wavepacket ansatz. The idea of the wavepacket equivalent source is to model the presence of extended coherent structures in the jet, with one goal of joining instability wave theory with

observed acoustics.[23,24] Although this test case (as with any acoustical inverse method) does not attempt to explain the fluid dynamics that produce the radiated jet noise, the analytically calculated sound field approximates important acoustic field characteristics found in the actual measurement of the full-scale jet sound field, such as the width and directivity of the maximum sound region and ground reflection interference nulls.[25] In addition, the input hologram for the M-SONAH algorithm for the simulated field corresponds to the microphone locations in the actual full-scale measurements[10] – a more limited aperture relative to the source simulated in Sec. IIIA. The hologram consists of 13 vertical points (from about 0.4 m height to 2.2 m height) by 153 points extending parallel to the assumed jet shear layer (see the solid white line in Fig. 6). The reconstruction includes all points along the shear layer and in the jet's geometric near and mid-fields at the jet central axis height of $y = 1.9$ m (the z-axis is parallel to the jet axis and the ground, and the x-axis is perpendicular to the jet axis and parallel to the ground).

The M-SONAH processing here is defined as follows: the two sets of cylindrical wavefunctions have z-axes that are aligned with the jet axis at heights of $y = 1.9$ m and -1.9 m, respectively, and are calculated using Hankel functions of order $n = 0$. The two wavefunction sets' parameters are summarized in Table I. The maximum wavenumber amplitude $|k_z|_{max}$ is set by the axial sample spacing, and the axial aperture length, L_z, determines the wavenumber spacing Δk_z.

Table I. Parameters of the two wavefunction sets representing the direct and image source.

Direct source: $\psi_{k_z,n}(r, \varphi, z)$, where
$r \equiv \sqrt{x^2 + (y - 1.9\text{m})^2}$
$\phi \equiv \tan^{-1}\left(\frac{y-1.9\text{m}}{x}\right)$, four-quadrant arctangent in $(-\pi, \pi]$
$z \equiv z$
$n = 0$
$\Delta k_z = \pi/L_z$, $|k_z|_{max} = 2\pi/\Delta z$
Image source: $\psi'_{k_z,n}(r, \varphi, z)$, where
$r \equiv \sqrt{x^2 + (y + 1.9\text{m})^2}$
$\phi \equiv \tan^{-1}\left(\frac{y+1.9\text{m}}{\sim}\right)$, four-quadrant arctangent in $(-\pi, \pi]$
$z \equiv z$
$n = 0$
$\Delta k_z = \pi/L_z$, $|k_z|_{max} = 2\pi/\Delta z$

The resulting M-SONAH intensity field reconstructions well match the simulated field. The reconstructed intensity field of a horizontal plane at the height of the engine nozzle, y = 1.9 m is displayed in Fig. 6(a). The reconstructed intensity magnitude is indicated by the length of the vector arrows which are cube-root scaled for convenience, and the color map indicates reconstructed level. The magnitude or angle errors between this M-SONAH reconstruction and the simulated field are shown in Fig. 6(b)-(c), respectively. As in Sec. IIIA, reconstructed L_I error is less than 3 dB and angle error is less than 10⁰ for the region where the simulated L_I is within 20 dB of maximum value. Larger magnitude and angle errors are mostly confined to areas outside of the input hologram plane (shown by the solid line in each part of Fig. 6), indicative of the effect of a finite measurement aperture. For example, the region where magnitude error exceeds 10 dB, near $z = 25$-30 m in Fig. 6(b), appears beyond the edge of the measurement plane.

In light of this test case, one quantitative way to validate the intensity reconstructions is to discard intensity reconstructions with magnitude less than that captured at the edges of the measurement aperture. In this case, this criterion would leave only the top 23 dB of intensity magnitude towards the right edge and the top 40 dB towards the left of the aperture, as illustrated by the dashed lines. Nearly all points where the magnitude error exceeds 3 dB or the angle error exceeds 10⁰ lie outside this region.
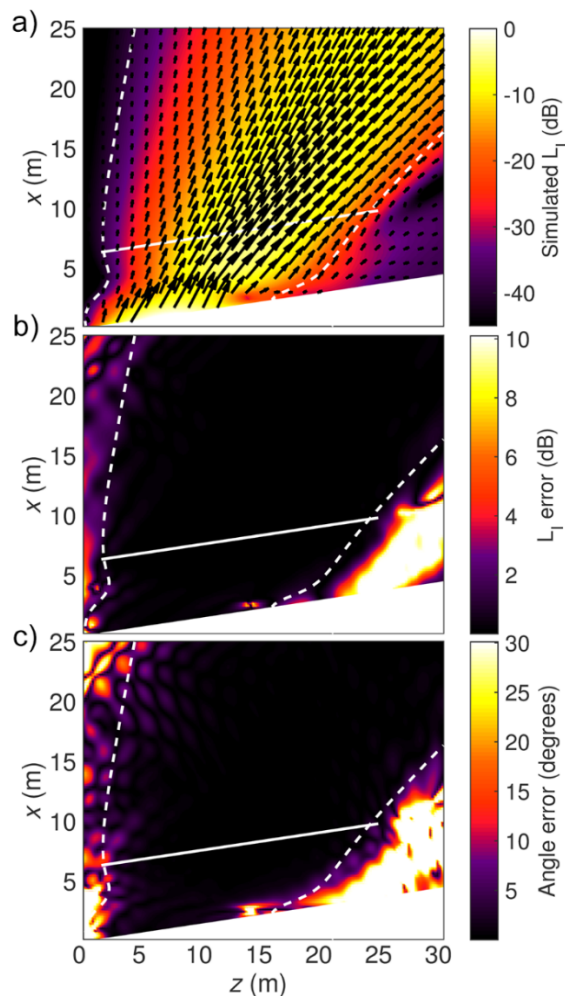
Figure 6. M-SONAH reconstructed intensity field (a), and errors in level (b) and angle errors (c) between the reconstruction and simulated fields, from the wavepacket-like line sources. A solid line is placed at the simulated hologram location (the hologram is a plane that extends vertically into and out of the page). Dashed contours trace the locations with the same L_I that the measurement aperture edges recorded. Note how at nearly all points within the contours level error is < 3 dB and angle error is < 10°.

4. CONCLUSION

In this paper, a modified SONAH algorithm using multiple sets of wavefunctions (termed M-SONAH)[9,10] has been extended for particle velocity and vector intensity reconstructions and tailored towards jet noise measurements in the presence of a rigid reflecting surface. The algorithm has been tested against two analytical test case scenarios, with a pair of line sources representing a model jet source and image source. The first scenario confirms the accuracy of M-SONAH intensity reconstructions at locations both nearer to and farther from the source with respect to the hologram, with highest accuracy in the regions with the largest intensity magnitudes. The second scenario uses a wavepacket model to approximate important features of a full-scale jet noise measurement such as lobe width, ground reflection interference, and a finite measurement aperture. Results suggest again that the highest levels of reconstructed intensity are the most accurate and that intensity reconstructions with magnitude less than that captured at the measurement aperture edges should be discarded.

ACKNOWLEDGMENTS

REFERENCES

[1] P. Kuronen, E. Toppila, J. Starck, R. Paakkonen, and M. J. Sorri, "Modelling the risk of noise-induced hearing loss among military pilots," Int. J. Audiology **43** (2), 79-84 (2004).

[2] J. Laufer, R. Schlinker, and R. E. Kaplan, "Experiments on supersonic jet noise," AIAA J. **14** (4), 489-497 (1976).

[3] C. K. W. Tam, K. Viswanathan, K. K. Ahuja, and J. Panda, "The sources of jet noise: experimental evidence," J. Fluid Mech. **615** (1), 253-292 (2008).

[4] J. Panda, and R. Mosher, "Use of a microphone phased array to determine noise sources in a rocket plume," 49th Aerospace Sci. Mtg., AIAA Paper 2011-974 (2011).

[5] S. Dumbacher, J. Blough, D. Hallman, and P. Wang, *Source identification using acoustic array techniques*, SAE Technical Paper, No. 951360 (1995).

[6] R. Steiner and J. Hald, "Near-field acoustical holography without the errors and limitations caused by the use of spatial DFT," Int. J. Sound Vib. **6** (2), 83-89 (2001).

[7] J. Hald, "Basic theory and properties of statistically optimized near-field acoustical holography," J. Acoust. Soc. Am. **125** (4), 2105-2120 (2009).

[8] Y. T. Cho, J. S. Bolton and J. Hald, "Source visualization by using statistically optimized near-field acoustical holography in cylindrical coordinates," J. Acoust. Soc. Am. **118** (4), 2355 (2005).

[9] A. T. Wall, K. L. Gee, and T. B. Neilsen, "Multisource statistically optimized near-field acoustical holography," J. Acoust. Soc. Am. **137** (2), 963-975 (2015).

[10] A. T. Wall, K. L. Gee, T. B. Neilsen, R. L. McKinley, and M. M. James, "Military jet noise source imaging using multisource statistically optimized near-field acoustical holography," J. Acoust. Soc. Am. **139** (4), 1938-1950 (2016).

[11] J. D. Maynard, E. G. Williams, and Y. Lee, "Neafield acoustic holography: I. Theory of generalized holography and the development of NAH," J. Acoust. Soc. Am. **74** (4), 1395-1413, (1985).

[12] M. Lee and J. S. Bolton, "Source characterization of a subsonic jet by using near-field acoustical holography," J. Acoust. Soc. Am. **121** (2), 967-977 (2007).

[13] J. Hald, "Patch holography in cabin environments using a two-layer hand-held array and an extended SONAH algorithm," Proceedings of Euronoise 2006 (2006).

[14] A. T. Wall, K. L. Gee, T. B. Neilsen, D. W. Krueger, M. M. James, S. D. Sommerfeldt and J. D. Blotter, "Full-scale jet noise characterization using scan-based acoustical holography," AIAA Paper 2012-2081 (2012).

[15] M. Lee, J. S. Bolton, and L. Mongeau, "Application of cylindrical near-field acoustical holography to the visualization of aeroacoustic sources," J. Acoust. Soc. Am. **114** (2), 842-858 (2003).

[16] J. Hald, "Scaling of plane-wave functions in statistically optimized near-field acoustic holography," J. Acoust. Soc. Am. **136** (5), 2687-2696 (2014).

[17] F. Jacobsen, and V. Jaud, "Statistically optimized near field acoustic holography using an array of pressure-velocity probes," J. Acoust. Soc. Am. **121** (3), 1550-1558 (2007).

[18] J.-C. Pascal, T. Loyau, and J. A. Mann III, "Structural intensity from spatial Fourier transformation and BAHIM acoustical holography method," Proc. Cong. On Structural Intensity and Vibrational Energy Flow, 197-204, (1990).

[19] J. Hald, "Patch near-field acoustical holography using a new statistically optimal method," Proc. INTER-NOISE, Paper 2203–2210 (2003).

[20] E. G. Williams, "Regularization methods for near-field acoustical holography," J. Acoust. Soc. Am. **110** (4), 1976-1988 (2001).

[21]E. G. Williams, *Fourier acoustics: Sound radiation and nearfield acoustical holography,* (Academic Press, San Diego, 1999).

[22]D. Papamoschou, "Wavepacket modeling of the jet noise source," AIAA Paper 2011-2835, (2011).

[23]R. Reba, S. Narayanan, T. Colonius, and T. Suzuki, "Modeling jet noise from organized structures using near-field hydrodynamic pressure," AIAA Paper 2005-3093 (2005).

[24]K. Gudmundsson, and T. Colonius. "Instability wave models for the near-field fluctuations of turbulent jets," J. Fluid Mech. **689,** 97-128 (2011).

[25]A. T. Wall, K. L. Gee, T. B. Neilsen, B. M. Harker, S. A. Mcinerny, R. L. McKinley, and M. M. James, "Investigation of multi-lobed fighter jet noise sources using acoustical holography and partial field decomposition methods," AIAA paper 2015-2379 (2015).